DECIPHERING THE IONIZED GAS CONTENT IN THE MASSIVE STAR-FORMING COMPLEX G75.78+0.34

Álvaro Sánchez-Monge[1,2,3], Stan Kurtz[3], Aina Palau[4], Robert Estalella[2], Debra Shepherd[5],
Susana Lizano[3], José Franco[6], and Guido Garay[7]

[1] Osservatorio Astrofisico di Arcetri, INAF, Largo E. Fermi 5, I-50125 Firenze, Italy; asanchez@arcetri.astro.it
[2] Dpt d'Astronomia i Meteorologia (IEEC-UB), Institut de Ciències del Cosmos, Universitat de Barcelona, Martí i Franquès, 1, E-08028 Barcelona, Spain
[3] Centro de Radioastronomía y Astrofísica, Universidad Nacional Autónoma de México, Apdo. Postal 3-72, 58090, Morelia, Michoacán, Mexico
[4] Institut de Ciències de l'Espai (CSIC-IEEC), Campus UAB–Facultat de Ciències, Torre C5p 2, E-08193 Bellaterra, Catalunya, Spain
[5] NRAO, P.O. Box O, Socorro, NM 87801-0387, USA
[6] Instituto de Astronomía, Universidad Nacional Autónoma de México, Apdo. Postal 70-264, 04510 México, D.F., Mexico
[7] Departamento de Astronomía, Universidad de Chile, Camino el Observatorio 1515, Las Condes, Santiago, Chile

ABSTRACT

We present subarcsecond observations toward the massive star-forming region G75.78+0.34. We used the Very Large Array to study the centimeter continuum and H_2O and CH_3OH maser emission, and the Owens Valley Radio Observatory and Submillimeter Array to study the millimeter continuum and recombination lines (H40α and H30α). We found radio continuum emission at all wavelengths, coming from three components: (1) a cometary ultracompact (UC) H II region with an electron density $\sim 3.7 \times 10^4$ cm^{-3}, excited by a B0 type star, and with no associated dust emission; (2) an almost unresolved UCH II region (EAST), located $\sim 6''$ to the east of the cometary UCH II region, with an electron density $\sim 1.3 \times 10^5$ cm^{-3}, and associated with a compact dust clump detected at millimeter and mid-infrared wavelengths; and (3) a compact source (CORE), located $\sim 2''$ to the southwest of the cometary arc, with a flux density increasing with frequency, and embedded in a dust condensation of 30 $M_\odot$. The CORE source is resolved into two compact and unresolved sources which can be well fit by two homogeneous hypercompact H II regions each one photoionized by a B0.5 zero-age main sequence star, or by free–free radiation from shock-ionized gas resulting from the interaction of a jet/outflow system with the surrounding environment. The spatial distribution and kinematics of water masers close to the CORE-N and S sources, together with excess emission at 4.5 μm and the detected dust emission, suggest that the CORE source is a massive protostar driving a jet/outflow.

Key words: dust, extinction – H II regions – ISM: individual objects (G75.78+0.34) – radio continuum: ISM – stars: formation

Online-only material: color figures

1. INTRODUCTION

Massive stars are key to understanding many physical phenomena in the Galaxy, however their first stages of formation are still poorly understood. One of the main reasons is that massive stars evolve more quickly to the main sequence than low-mass stars, and they radiate large amounts of ultraviolet (UV) photons and drive strong winds while they are still deeply embedded and accreting matter (e.g., Beuther & Shepherd 2005; Keto 2007). The interaction of the UV radiation and winds with the surrounding environment, resulting in bright radio continuum sources, must be well understood to comprehend the formation of high-mass stars.

Thermal (free–free) radio emission at centimeter wavelengths in regions of massive star formation can have distinct origins: (1) H II regions photoionized by embedded massive stars, with homogeneous density distributions (e.g., Mezger & Henderson 1967) or with density gradients (e.g., Olnon 1975; Panagia & Felli 1975; Franco et al. 2000); (2) clumps of gas or circumstellar disks externally ionized by luminous early-type stars (e.g., Garay 1987; O'Dell & Wong 1996; Zapata et al. 2004); (3) shock waves arising either in dense interstellar gas (e.g., Ghavamian & Hartigan 1998; Araya et al. 2009) or from the collision of thermal radio jets from young stellar objects (YSOs) with their surroundings (e.g., Anglada 1996; Eisloffel et al. 2000; Rodríguez et al. 2005); (4) ionized accretion flows where the material becomes ionized while accreting onto the massive protostar (e.g., Keto 2002, 2003, 2007); (5) photoevaporated disks where the radiation of the newly formed star ionizes and evaporates the surrounding disk (e.g., Hollenbach et al. 1994; Lugo et al. 2004; Ávalos & Lizano 2012); (6) equatorial winds with the emission produced by small-scale ionized stellar winds (e.g., Hoare 2006). All these mechanisms produce radio continuum sources with spectral indices, α ($S_\nu \propto \nu^\alpha$), between -0.1 and $+2$ (i.e., thermal emission; see Rodríguez et al. 1989). In addition, several works have found negative spectral indices (typical of non-thermal emission) associated with massive YSOs (e.g., Rodríguez et al. 1989; Zapata et al. 2006). These non-thermal sources can be young stars with active magnetospheres producing gyro-synchrotron emission (e.g., Feigelson & Montmerle 1999); synchrotron emission from fast shocks in disks or jets (e.g., Reid et al. 1995; Shepherd & Kurtz 1999; Shchekinov & Sobolev 2004); or extremely embedded YSOs where the UV photons from the massive protostars are heavily absorbed by large amounts of dust, with mass column densities $\gtrsim 10^3$ g cm^{-2} (Rodríguez et al. 1993). A similar description of these mechanisms producing centimeter continuum emission can be found in Rodríguez et al. (2012).

It is possible—and indeed, probable—that several of these emission mechanisms, either thermal or non-thermal, occur within massive star formation regions, either simultaneously or at different evolutionary epochs. Any complete model of high-mass star formation must address the presence of these multiple modes of radio continuum emission.

Table 1
Main Continuum Observational Parameters of G75.78+0.34

λ (cm)	Telescope	Project	Epoch of Observation	Phase Calibrator / Bootstrapped Flux[a]	Flux Calibrator	Beam ($'' \times ''$)	P.A. ($^\circ$)	rms (mJy beam^{-1})
6.0	VLA-B	AF381	2001 Apr 23	2015+371/2.50(1)	3C48	1.6 × 1.3	−87	0.49
3.6	VLA-B	AK440	1997 Mar 16	2025+337/3.50(1)	3C286	1.0 × 0.7	+6	0.14
3.6	VLA-A	AK490	1999 Sep 12+13	2015+371/2.01(1)	3C286	0.3 × 0.2	−73	0.05
2.0	VLA-CnB	AK423	1996 Jan 29	2025+337/2.72(2)	3C286	1.7 × 1.4	+66	0.36
2.0	VLA-B	AF381	2001 Apr 23	2015+371/2.62(1)	3C286	0.6 × 0.4	−84	0.11
1.3	VLA-B	AK440	1997 Mar 16	2025+337/3.48(2)	3C286	0.31 × 0.26	−14	0.12
1.3	VLA-A	AK490	1999 Sep 12+13	2015+371/1.82(2)	3C286	0.10 × 0.08	+52	0.13
0.7	VLA-CnB	AK423	1996 Jan 29	2025+337/2.33(2)	3C286	2.5 × 0.5	−64	0.46
0.7	VLA-B	AK500	1999 + 2000	2015+371/2.10(4)	3C286	0.14 × 0.12	+37	0.25
0.31	OVRO		1997 + 1998	BL Lac/5.4(20)	Uranus	2.0 × 1.7	−88	0.59
0.13	OVRO		1997 Sep–Dec	BL Lac/2.5(30)	Uranus	1.6 × 1.5	−51	4.0
0.12	SMA	09B-S106	2010 Jun 10	2025+337/1.7(15)	Callisto	6.4 × 2.7	−76	8.4

Notes. [a] Bootstrapped flux density in Jy. The number in parentheses gives the uncertainty of the flux density as a percentage.

The ON-2 star-forming complex contains several early-type (O and B) stars within a massive ($\gtrsim 10^4\ M_\odot$; Matthews et al. 1986; Dent et al. 1988) molecular cloud that spans ∼10′ on the sky. Seen in CO, the cloud has two distinct condensations, with a roughly north–south orientation (Matthews et al. 1986). Multiple ionized regions within the southern condensation were identified by Matthews et al. (1973, 1977). They reported an extended H II region G75.77+0.34, and also the ultracompact (UC) H II region G75.78+0.34 (hereafter G75); the latter is associated with strong OH maser emission first reported by Elldér et al. (1969).

ON-2 lies toward Cygnus-X, and hence it has been problematic to assign a reliable distance. Early estimates ranged from 0.9 to 5.5 kpc with the nearer distance coming from extinction or luminosity arguments and the farther distance coming from Galactic rotation models and radio recombination line (RRL) velocities. A helpful summary is presented by Campbell et al. (1982). More recent works, focusing on the UC H II region rather than the molecular cloud, tend to adopt a kinematic distance of 5.6 kpc (e.g., Wood & Churchwell 1989; Hanson et al. 2002). More recently, Ando et al. (2011) observed the water masers associated with the G75 UC H II region as part of the VERA (VLBI Exploration of Radio Astrometry) project. They measured the trigonometric parallax and report a heliocentric distance of 3.83 ± 0.13 kpc. We consider this distance measurement to be the most reliable and we adopt 3.83 kpc for our analysis. This distance places G75 close to other star-forming regions (G75.76+0.35 and AFGL 2591; Rygl et al. 2012), and close to the solar circle (Ando et al. 2011; Nagayama & VERA project members 2012).

At centimeter wavelengths, G75 is dominated by a cometary UCH II region reported by Wood & Churchwell (1989). Hofner & Churchwell (1996) detected a cluster of water masers located about 2″ (10^4 AU) southwest of the UCH II region, coincident with a compact radio continuum source (Carral et al. 1997) with a spectral index of +1.5 ± 0.4 from 6 cm through 3 mm. Franco et al. (2000) modeled this compact continuum source as a hypercompact (HC) H II region with $n_e \propto r^{-4}$. They note that this very steep density gradient is probably unrealistic, and mentioned several possible causes, including a contribution from warm dust to the flux density at 0.7 cm. Additionally, emission from a myriad of molecular line transitions has been reported in single-dish surveys (e.g., Shirley et al. 2003; Roberts & Millar 2007; Klaassen & Wilson 2007; Bisschop et al. 2007). Higher angular resolution observations of different dense gas

tracers show that most of the molecular emission comes from the compact radio continuum source associated with the cluster of water masers (Codella et al. 2010; Sánchez-Monge 2011). Finally, up to four distinct outflows have been identified in the ON-2 cloud core (Shepherd et al. 1997). All this makes G75 an excellent target to study the nature of the centimeter continuum sources in a massive star-forming region.

In this paper, we present high angular resolution centimeter continuum observations together with 22 GHz H_2O and 44 GHz CH_3OH maser observations toward G75. We complement this data with millimeter continuum and RRL observations, with the goal of deciphering the nature of the centimeter continuum sources.

2. OBSERVATIONS

2.1. VLA Radio Continuum Observations

G75.78+0.34 was observed with the Very Large Array (VLA[8]) at 6.0, 3.6, 2.0, 1.3, and 0.7 cm from 1996 January to 2001 April, using the array in the CnB, B, and A configurations. In Table 1, we summarize these observations. The data reduction followed standard procedures for calibration of high-frequency data, using the NRAO package AIPS. Initial images were produced with a robust parameter (Briggs 1995) of 1 (see Table 1 for synthesized beams and rms noise levels of these images). These data can be grouped into two categories based on angular resolution: those with $\theta_{\rm beam} \geqslant 1''.0$, and those with $\theta_{\rm beam} \sim 0''.2$. The continuum images at 1.3 cm and 0.7 cm, from projects AK490 and AK500, were cross-calibrated with the strongest H_2O and CH_3OH maser components, respectively, which were observed simultaneously with the continuum emission (see Section 2.2 and Table 2). After comparing the initial maps for consistency, we combined the uv-data at the same frequencies to obtain final images with better uv-coverage and sensitivity. The resulting synthesized beams and rms noise levels of the combined images are given in Table 3.

At 6 cm, the H II region G75.77+0.34, approximately 1′ to the southwest (e.g., Riffel & Lüdke 2010), produced non-imageable artifacts. The shortest baselines (<5 kλ) were excluded, producing essentially no change in the measured flux density but significantly improving the quality of the map.

---

[8] The National Radio Astronomy Observatory is a facility of the National Science Foundation operated under cooperative agreement by Associated Universities, Inc.

Table 2
Main Observational Parameters of the VLA and OVRO Spectral Line Observations

Line	Frequency	Telescope	Bandwidth	Spectral Resolution		v_{ref}[a]	Beam	P.A.	rms
	(GHz)		(MHz)	(kHz)	(km s^{-1})	(km s^{-1})	($'' \times ''$)	(°)	(mJy beam^{-1})
H_2O (6_{16}–5_{23})	22.235080	VLA	1.56	24.4	0.33	+1.	0.07 × 0.07	−67	77.
		VLA	6.25	97.7	1.3	−10.	0.10 × 0.07	−69	50.
CH_3OH (7_0–6_1)	44.069410	VLA	1.56	24.4	0.17	+3.	0.11 × 0.10	+32	30.
H40α	99.022960	OVRO	128.	2000.	6.1	−8.	5.6 × 2.8	+33	10.
H30α	231.900940	OVRO	128.	2000.	2.6	−8.	3.9 × 1.8	+29	15.

Notes. [a] Central velocity of the passband in the local standard of rest.

Table 3
Multiwavelength Results for the YSOs in the Star-forming Region G75.78+0.34

Wavelength	Beam	P.A.	rms	I_ν^{peak}[a]	S_ν[a]	Deconv. Size	P.A.
(cm)	($'' \times ''$)	(°)	(μJy beam^{-1})	(mJy beam^{-1})	(mJy)	($'' \times ''$)	(°)
UCH II	$\alpha(J2000.0) = 20^h21^m44\overset{s}{.}098$[b]						
	$\delta(J2000.0) = +37°26'39\overset{''}{.}47$[b]						
6.0	1.30 × 1.11	+89	485	24 ± 1	49 ± 6	1.3 × 1.2 ± 0.4	60 ± 40
3.6	0.33 × 0.26	−75	61	3 ± 1	32 ± 4	1.0 × 0.8 ± 0.1	70 ± 10
2.0	0.60 × 0.40	−69	138	7 ± 1	34 ± 4	1.1 × 0.9 ± 0.1	70 ± 10
1.3	0.19 × 0.19	+33	67	2 ± 1	32 ± 4	1.0 × 0.9 ± 0.1	80 ± 10
0.7	0.35 × 0.33	−74	159	4 ± 1	27 ± 4	1.2 × 0.8 ± 0.2	75 ± 10
0.31	1.96 × 1.74	−88	579	21 ± 2	34 ± 14	2.0 × 0.8 ± 0.3	120 ± 10
0.13	1.61 × 1.49	−51	4000	...	<16	...	...
EAST	$\alpha(J2000.0) = 20^h21^m44\overset{s}{.}499$[b]						
	$\delta(J2000.0) = +37°26'37\overset{''}{.}80$[b]						
6.0	1.30 × 1.11	+89	485	4.1 ± 1.0	4.5 ± 1.5	1.3 × 1.0 ± 0.7	130 ± 50
3.6	0.33 × 0.26	−76	61	2.9 ± 0.2	4.5 ± 0.6	0.25 × 0.20 ± 0.04	135 ± 40
2.0	0.60 × 0.40	−69	138	3.8 ± 0.3	3.9 ± 0.7	0.15× < 0.3 ± 0.15	105 ± 40
1.3	0.19 × 0.19	+33	67	2.2 ± 0.2	3.9 ± 0.6	0.20 × 0.15 ± 0.05	90 ± 20
0.7	0.35 × 0.33	−74	159	2.9 ± 0.4	3.3 ± 0.7	0.2 × 0.1 ± 0.2	90 ± 50
0.31	1.96 × 1.74	−88	579	6.0 ± 1.2	9.9 ± 4.7	2.8 × 1.7 ± 0.5	25 ± 20
0.13	1.61 × 1.49	−51	4000	...	<17	...	...
CORE	$\alpha(J2000.0) = 20^h21^m44\overset{s}{.}030$[b]						
	$\delta(J2000.0) = +37°26'37\overset{''}{.}67$[b]						
6.0	1.30 × 1.11	+89	485	...	<1.9	...	...
3.6	0.33 × 0.26	−76	61	0.8 ± 0.2	1.4 ± 0.3	...	...
2.0	0.60 × 0.40	−69	138	2.1 ± 0.3	3.1 ± 0.7	0.45 × 0.23 ± 0.09	50 ± 20
1.3	0.19 × 0.19	+33	67	2.2 ± 0.2	4.8 ± 0.7	...	...
0.7	0.35 × 0.33	−74	159	4.0 ± 0.3	7.9 ± 1.2	0.6 × 0.2 ± 0.1	55 ± 15
0.31	1.96 × 1.74	−88	579	23 ± 2	36 ± 14	2.0 × 1.4 ± 0.3	145 ± 10
0.13	1.61 × 1.49	−51	4000	98 ± 10	300 ± 100	4.0 × 2.2 ± 0.3	145 ± 10
CORE-N	$\alpha(J2000.0) = 20^h21^m44\overset{s}{.}041$[b]						
	$\delta(J2000.0) = +37°26'37\overset{''}{.}76$[b]						
3.6	0.33 × 0.26	−76	61	0.8 ± 0.2	0.8 ± 0.2	0.4 × 0.1 ± 0.1	50 ± 20
2.0	0.43 × 0.35	−84	144	2.0 ± 0.3	2.1 ± 0.5	0.4 × 0.1 ± 0.1	50 ± 15
1.3	0.19 × 0.19	+33	67	2.2 ± 0.2	2.7 ± 0.4	0.15 × 0.08 ± 0.04	30 ± 10
0.7	0.15 × 0.13	+40	186	2.6 ± 0.4	2.6 ± 0.8	0.05× < 0.07 ± 0.05	55 ± 30
CORE-S	$\alpha(J2000.0) = 20^h21^m44\overset{s}{.}016$[b]						
	$\delta(J2000.0) = +37°26'37\overset{''}{.}55$[b]						
3.6	0.33 × 0.26	−76	61	0.6 ± 0.2	0.6 ± 0.2	0.5 × 0.1 ± 0.1	55 ± 15
2.0	0.43 × 0.35	−84	144	1.8 ± 0.3	1.8 ± 0.5	0.4 × 0.1 ± 0.1	50 ± 15
1.3	0.19 × 0.19	+33	67	1.9 ± 0.2	2.1 ± 0.4	0.20 × 0.07 ± 0.05	45 ± 10
0.7	0.15 × 0.13	+40	186	2.7 ± 0.4	3.2 ± 0.9	0.10 × <0.07 ± 0.05	100 ± 30

Notes.
[a] Primary beam corrected. Error in intensity is 2σ. Error in flux density has been calculated as $[(2\sigma\,(\theta_{source}/\theta_{beam})^{1/2})^2 + (2\sigma_{flux-scale})^2]^{1/2}$, where σ is the rms noise level of the map, θ_{source} and θ_{beam} are the size of the source and the beam, respectively, and $\sigma_{flux-scale}$ is the error in the flux scale, which takes into account the uncertainty on the calibration applied to the flux density of the source ($S_\nu \times \%_{uncertainty}$).
[b] Coordinates calculated as an average of the coordinates at each wavelength where the source is well detected (i.e., not filtered out). Typical discrepancies in the coordinates at different wavelengths are <0$\overset{''}{.}$1.

2.2. VLA H_2O and CH_3OH Maser Observations

The water maser line at 22.23508 GHz (6_{16}–5_{23} transition) was observed with the VLA in the A configuration (project AK490) simultaneously with the 1.3 cm continuum emission. Two different correlator configurations were used, providing spectral resolutions of 0.3 and 1.3 km s^{-1}, with velocity coverages of 21 and 83 km s^{-1}, respectively.

The class I methanol maser line at 44.06941 GHz (7_0–6_1 A$^+$ transition) was observed with the VLA in the B configuration (project AK500) simultaneously with the 0.7 cm continuum emission. Details of the spectrometer configuration are given in Table 2.

The H_2O and CH_3OH maser data were calibrated following the AIPS guidelines for calibration of high-frequency data. Self-calibration was performed on the strongest maser component, and the solutions were applied to the spectral line and continuum data. The images were constructed using uniform and natural weighting to measure the maser positions at the highest angular resolution and to estimate the intensity of the different maser components, respectively.

2.3. OVRO Observations

The Owens Valley Radio Observatory (OVRO[9]) observations at 3 and 1 mm were made in the L (Low) and H (High) resolution configurations during 1997 September, October, and December. In 1998 March, additional 3 mm observations were made in the uH (ultra-High) resolution configuration. All the observations were made in the double sideband mode, simultaneously observing at 3 and 1 mm. The continuum was observed in two 1 GHz channels, centered at 95.78 GHz and 98.78 GHz for 3 mm and 228.85 GHz and 231.85 GHz for 1 mm.

In addition, spectral line modules covered the H40α (99.02296 GHz) and H30α (231.90094 GHz) RRLs. Each spectral line set-up consisted of 62 Hanning smoothed channels of 2 MHz each, providing resolutions of 6.1 and 2.6 km s^{-1} at 3 mm and 1 mm, respectively. The assumed local standard of rest (LSR) velocity for both lines was −8 km s^{-1}. Bandpass calibration was performed by observing the quasar 3C454.3. Amplitude and phase calibration were achieved by monitoring BL Lac during the different observing tracks. The absolute flux density scale was determined from Uranus, with an estimated uncertainty of 20% at 3 mm and 30% at 1 mm. The data were reduced using a combination of routines from the OVRO reduction package MMA, from MIRIAD, and from AIPS. Imaging was performed with the task IMAGR of AIPS. In Tables 1 and 2, we list details of the continuum and RRL observations.

2.4. SMA Observations

G75.78+0.34 was observed with the Submillimeter Array (SMA[10]) in the 1.3 mm (230 GHz) band using the compact configuration on 2010 June 10. A total bandwidth of 2 × 4 GHz was used, covering the frequency ranges 218.2–222.2 GHz and 230.2–234.3 GHz, with a spectral resolution of ∼1 km s^{-1}. System temperatures ranged between 150 and 250 K. The zenith opacities at 225 GHz were around 0.10 and 0.15 during the

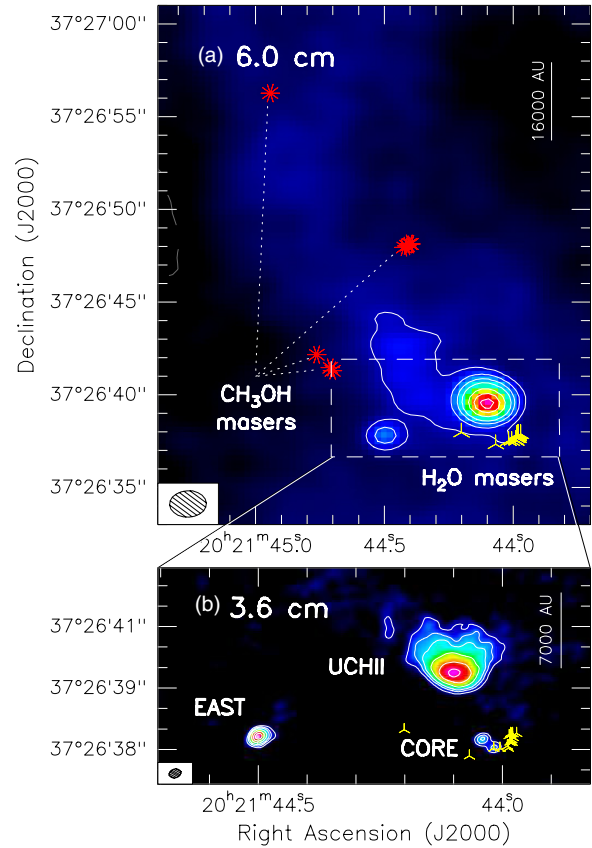**Figure 1.** G75.78+0.34 star-forming region. (a) VLA 6.0 cm continuum image. Levels are −3, 3, 6, 10, 15, 25, 35, 45, and 55 times 490 μJy beam^{-1}. Ten-point red stars indicate CH_3OH masers, and three-point yellow stars indicate H_2O masers. The dashed box shows the region zoomed in the bottom panel. (b) VLA 3.6 cm continuum image. Levels are −4, 4, 8, 12, 20, 30, and 40 times 50 μJy beam^{-1}. Synthesized beams of the continuum images are shown in the bottom-left corner; spatial scales are indicated in the top-right corner of each panel.

(A color version of this figure is available in the online journal.)

3 hr track. The FWHM of the primary beam at 1.3 mm was ∼56″. Bandpass calibration was performed by observing the quasar 3C454.3. Amplitude and phase calibrations were made by monitoring 2025+337 and 2015+371, with an rms phase of ∼40°. The absolute flux density scale was determined from Callisto with an estimated uncertainty around 15%. Data were calibrated and imaged with the MIRIAD software package. The continuum was constructed in the (u, v) domain from the line-free channels. Imaging was performed using natural weighting, resulting in a synthesized beam of 6″.4 × 2″.7 with a P.A. = −76°, and 1σ rms of 8.4 mJy beam^{-1} for the continuum. The two 4 GHz passbands include several molecular transitions, including CO, CH_3CN, and CH_3CCH. These molecular line data will be presented in a forthcoming paper together with VLA ammonia observations (A. Sánchez-Monge et al., in preparation).

3. RESULTS

3.1. Centimeter Continuum Emission

We detected centimeter radio continuum emission at all wavelengths. In Figure 1, we show a global overview of the G75 region at 6.0 cm (panel (a)) and 3.6 cm (panel (b)). As seen in the figure, the centimeter continuum emission is dominated by three components that we name UCHII, EAST, and CORE.
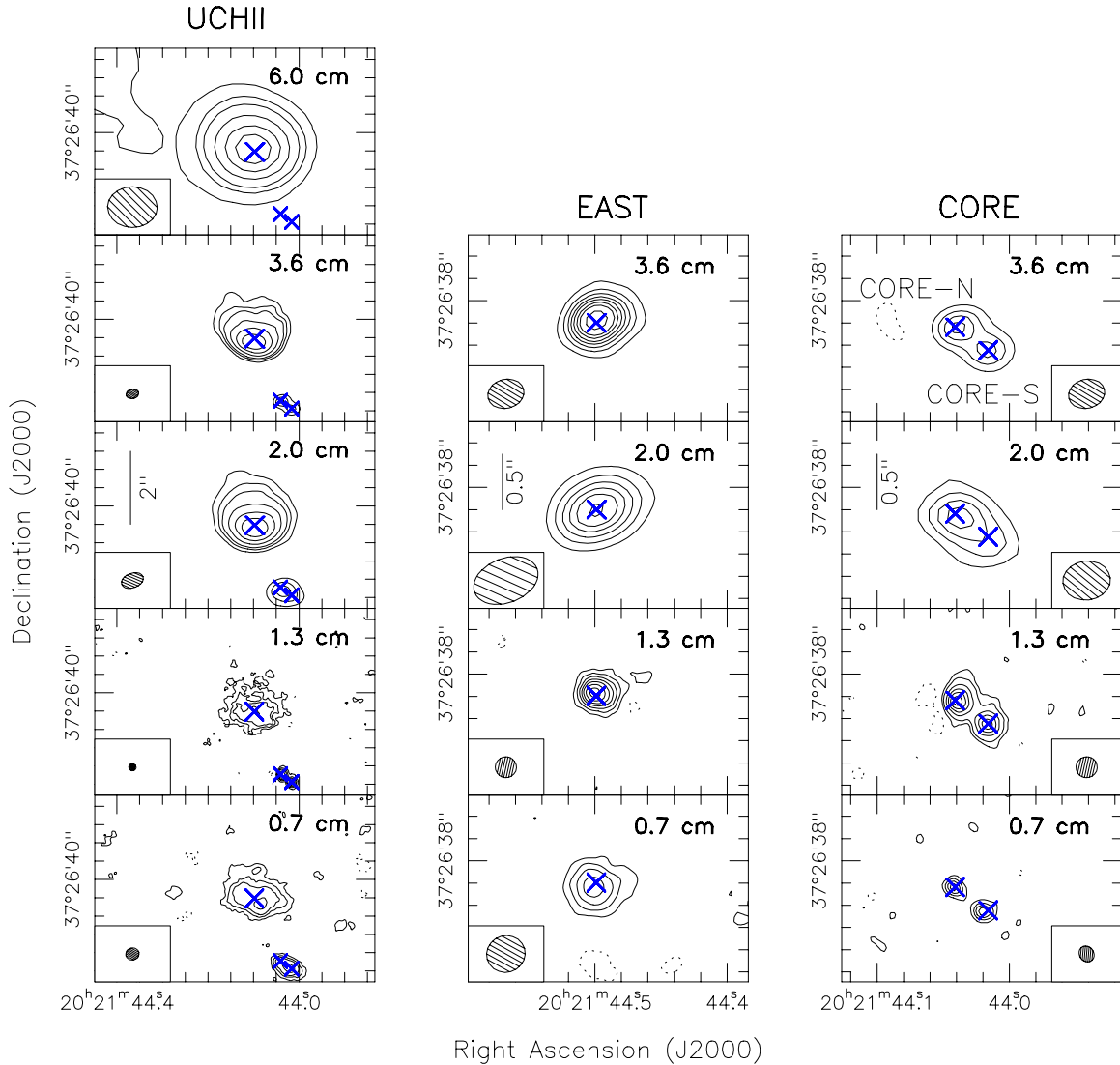
Figure 2. Close-up continuum images of the UCHII, EAST, and CORE sources. In each panel, we show the VLA image at the wavelength indicated in the top-right corners. Left column: UCHII source. For all panels, levels are −4, 4, 8, 12, 20, 30, and 40 times the rms noise level of the map: 485, 61, 138, 67, and 159 μJy beam^{-1}, for 6.0, 3.6, 2.0, 1.3, and 0.7 cm maps, respectively. Center column: EAST source. For all panels, levels are −4, 4, 8, 12, 16, 20, 25, and 30 times the rms noise level of the map: 61, 138, 67, and 159 μJy beam^{-1}, for 3.6, 2.0, 1.3, and 0.7 cm maps, respectively. Right column: CORE (N and S) source. For all panels, levels are −3, 3, 6, 12, 18, 24, and 30 times the rms noise level of the map: 61, 144, 67, and 186 μJy beam^{-1}, for 3.6, 2.0, 1.3, and 0.7 cm maps, respectively. See Table 3 for details of the synthesized beams, and the flux densities and sizes of the sources. Blue crosses in all panels indicate the position of the four continuum sources: UCHII, EAST, CORE-N, and CORE-S (see Table 3). The scale in arcseconds is shown in the 2.0 cm panels. At the adopted distance of 3.8 kpc, 2″ corresponds to 7600 AU while 0″.5 is 1900 AU.

(A color version of this figure is available in the online journal.)

In Figure 2, we show a close-up of these three sources for the combined maps at each frequency, and in Table 3 we list their flux densities and sizes, together with the beams, and rms noise levels of the combined images.

The strongest source (UCHII; G75.7826+0.3429) is a cometary UCH II region with an integrated flux density of ∼35 mJy and an angular diameter of ∼1″ (∼0.02 pc at a distance of 3.8 kpc; previously imaged by Wood & Churchwell 1989 and Carral et al. 1997). Located ∼6″ to the east, we identify a compact source (EAST; G75.7830+0.3416), with a flux density of ∼4 mJy and an angular diameter of ∼0″.2 (∼760 AU at a distance of 3.8 kpc). This source appears at the ∼5σ level in the 7 mm maps of Carral et al. (1997). Finally, at the head of the cometary arc we find a compact source (CORE; G75.7821+0.3418) slightly elongated in the northeast–southwest direction, with a flux density of a few mJy and increasing with frequency.

This source is coincident with the 7 mm continuum source reported by Carral et al. (1997) and with the clump of H$_2$O masers (Hofner & Churchwell 1996). Our higher angular resolution observations (≤0″.3) allow us to resolve the CORE source into two distinct (marginally resolved) condensations: CORE-N (G75.7821+0.3428) and CORE-S (G75.7820+0.3429; see Figure 2).

3.2. Millimeter Continuum Emission

In Figure 3, we show the OVRO and SMA millimeter continuum images of the G75 region. At 3.1 mm, we detect emission from all three sources, with the emission from the UCHII and CORE sources barely resolved. At 1.3 mm, we only detect emission associated with the CORE source, probably due to a lack of sensitivity that precludes the detection of
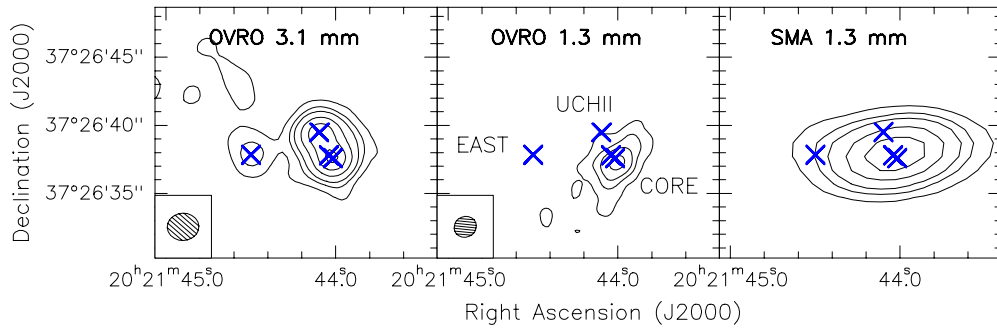
Figure 3. OVRO and SMA millimeter continuum maps. Levels are −4, 4, 8, 12, 20, 30, and 40 times the rms noise level of the map: 0.6, 4, and 8.4 mJy beam^{-1}, for OVRO 3.1 mm, OVRO 1.3 mm, and SMA 1.3 mm maps, respectively. See Table 3 and Section 3.2 for details of the flux and beam of each image. Blue crosses show the position of the radio-continuum sources, as in Figure 2.

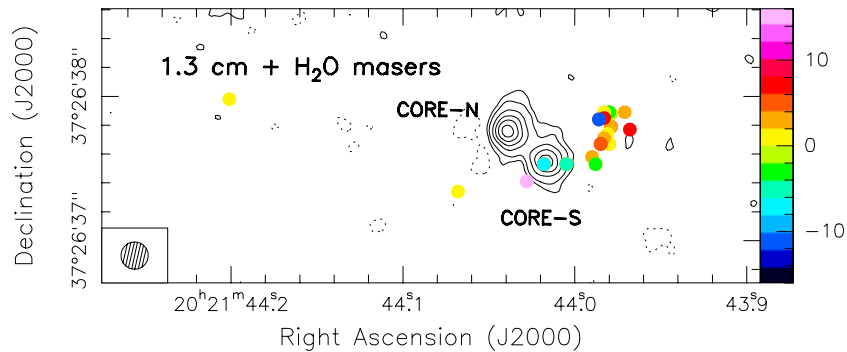(A color version of this figure is available in the online journal.)

Figure 4. H$_2$O maser distribution in G75. Black contours: VLA 1.3 cm continuum image as in Figure 2—right column. Color circles show the position of the 35 water maser spots (see Table 4). Different colors are used to indicate the maser LSR velocities, according to the color scale (in km s^{-1}) on the right-hand side of the plot.

(A color version of this figure is available in the online journal.)

faint emission from the EAST and UCHII sources. The angular resolution of our millimeter continuum images (10–15 times poorer than the angular resolution at centimeter wavelengths) does not allow us to resolve the components CORE-N and CORE-S. In Table 3, we list the flux densities and sizes, and the beams and rms noise levels of the OVRO observations. For the SMA 1.3 mm source, we fit a two-dimensional Gaussian obtaining a primary beam corrected flux density of 0.60 ± 0.17 Jy with a deconvolved size of $(4 \times 2 \pm 1)''$ at a P.A. = $(75 \pm 10)°$. The SMA 1.3 mm source, although centered on the CORE position, encompasses the UCHII source and shows an extension to the EAST source. In addition, the flux density measured in the SMA image is almost twice the flux density measured in the OVRO image, suggesting that there is some faint, extended emission not detected in the OVRO map. We refrain from combining the OVRO and SMA 1.3 mm continuum images because of the poorer uv-coverage and sensitivity of the latter. Higher sensitivity maps are needed to confirm the 1 mm continuum emission associated with the UCHII and EAST sources, and higher angular resolution is needed to identify the millimeter emission of CORE-N and S sources.

At 3.5 mm, Riffel & Lüdke (2010) measured a flux density of 119 mJy with a synthesized beam of $18''$, while Shepherd et al. (1997) measured 75 mJy with a resolution of $5''$, both observations made with the BIMA telescope. Our measurement ($\sim$75 mJy, including all the flux at 3.1 mm) is in good agreement with that of Shepherd et al. but somewhat lower than that of Riffel & Lüdke. This difference may arise because the latter work (with $18''$ resolution) was more sensitive to weak, extended emission.

3.3. H$_2$O and CH$_3$OH Maser Emission

Hofner & Churchwell (1996) reported a cluster of water masers located $2''$ southwest from the UCH II region, at the same position as the CORE source (as reported by Carral et al. 1997). Our H$_2$O maser observations at 22.235 GHz have a double aim: to cross-calibrate the radio continuum data at 1.3 cm, and to observe the masers with higher angular resolution ($\sim$0$''$.1 versus $\sim$0$''$.4 of previous observations). Two different spectral resolutions ($\sim$0.3 and $\sim$1.3 km s^{-1}) were used to observe the H$_2$O maser emission, allowing us to look for maser components in a velocity range of $(-40, +40)$ km s^{-1}. In Figure 4, we show the different H$_2$O maser positions (colored circles) overlaid on the 1.3 cm continuum image. We detected a total of 35 spots with velocities ranging from -36 to $+14$ km s^{-1}. In Table 4, we list the position, intensity, velocity, and integrated intensity of each H$_2$O maser component, indicating in the last column at which spectral resolution the component was detected. The water masers appear to form an arc at a distance of $\sim$2$''$ from the head of the cometary UCH II region (cf. Figure 1), with only a few of them directly associated with the CORE-S continuum source. We note that there are no instrumental offsets to be considered between the 1.3 cm continuum and the H$_2$O maser images, since the observations were simultaneous. This arc distribution of the maser spots was also reported by Ando et al. (2011) with VERA observations at 10 mas scales. In Figure 4, we use different colors as an indicator of the velocity of the maser component. No clear velocity gradients are found in the H$_2$O maser emission, although most of them appear slightly redshifted with respect to the cloud velocity, $v_{\rm LSR} \approx 0$ km s^{-1} (Olmi & Cesaroni 1999; Codella et al. 2010). In Section 5.2, we

Table 4
22 GHz Water and 44 GHz Methanol Masers in G75.78+0.34

α(J2000.0) (h m s)	δ(J2000.0) (° ′ ″)	S_{peak} (Jy)	v_{peak} (km s^{-1})	$\int S dv$ (Jy km s^{-1})	Notes[a]
H$_2$O Maser Components					
20 21 43.968	37 26 37.77	0.3	+7.0	0.4	L
20 21 43.971	37 26 37.89	1.5	+3.0	1.7	H
20 21 43.979	37 26 37.79	3.9	+6.9	3.1	H
		15.0	+2.3	16.4	H, L
20 21 43.979	37 26 37.88	2.4	+0.0	1.4	H
		1.0	−0.8	1.3	L
20 21 43.980	37 26 37.67	4.5	+2.6	6.3	H
		0.2	+0.5	0.3	L
20 21 43.980	37 26 37.89	1.5	+0.5	2.0	L
		0.7	−2.6	0.6	H, L
20 21 43.990	37 26 37.58	7.5	+3.0	10.5	H, L
20 21 43.981	37 26 37.74	5.1	+1.7	2.6	H
20 21 43.983	37 26 37.71	122.0	+3.0	220.0	H
20 21 43.983	37 26 37.89	1.7	+1.3	0.9	H
20 21 43.983	37 26 37.85	53.0	+6.9	111.0	H, L
20 21 43.985	37 26 37.67	0.2	+6.9	0.12	H
		0.3	+4.6	0.6	H, L
20 21 43.986	37 26 37.84	6.5	+4.3	3.9	H, L
		0.6	−11.0	1.6	L
20 21 43.988	37 26 37.53	3.1	+0.3	2.5	H, L
		1.0	−2.3	1.0	H
20 21 44.005	37 26 37.53	0.6	+5.5	0.6	H, L
		1.1	+1.7	0.9	H
		7.2	−1.3	15.1	H, L
		15.0	−5.6	20.4	H, L
20 21 44.017	37 26 37.58	0.5	−30.0	0.7	L
		1.4	−36.0	1.8	L
20 21 44.018	37 26 37.53	47.0	+7.3	65.5	H, L
		0.4	+4.9	0.2	H
		2.7	+2.0	3.0	H
		56.0	−0.7	150.0	H, L
		3.7	−6.2	6.7	H, L
20 21 44.028	37 26 37.41	0.7	+14.0	0.9	L
20 21 44.068	37 26 37.34	2.3	+0.3	3.0	H, L
20 21 44.201	37 26 37.98	2.4	+0.7	2.4	H, L
CH$_3$OH Maser Components					
20 21 44.397	37 26 48.14	0.06	+1.3	0.04	1
20 21 44.403	37 26 48.15	0.07	−0.3	0.06	1
20 21 44.412	37 26 48.04	0.4	+1.3	0.4	1
20 21 44.424	37 26 47.96	1.6	+0.5	2.4	1
20 21 44.701	37 26 41.30	6.8	+3.8	5.6	2
20 21 44.710	37 26 41.47	1.2	+4.2	1.0	2
20 21 44.763	37 26 42.17	5.8	+3.2	6.7	3
20 21 44.943	37 26 56.28	1.8	+0.5	1.2	4

Notes. [a] Labels H and L (for water masers) refer to the VLA observations done with a spectral resolution of 0.33 km s^{-1} and 1.3 km s^{-1}, respectively. Numbers 1–4 (for methanol masers) refer to the four groups of methanol masers detected (see Figure 1, panel (a)).

discuss the possible association between water masers and the continuum emission.

Regarding the class I methanol masers at 44.069 GHz, we detect four general locations of emission (with a total of eight different components; see Figure 1, panel (a)). In Table 4, we list the position, intensity, velocity, and integrated intensity for all the methanol maser components. None of the 44 GHz CH$_3$OH spots appear to be directly associated with any of the radio continuum sources, but rather are located at a distance of 10″–20″ (0.2–0.4 pc for a distance of 3.8 kpc) to the northeast

of the three main YSOs. As in other star-forming regions (e.g., Kurtz et al. 2004), class I methanol masers rarely coincide with other signposts of star formation (e.g., H II regions, OH masers, class II methanol masers). Theoretical models of methanol masers suggest that the class I masers arise in an environment where collisional processes dominate (Cragg et al. 1992; Pratap et al. 2008). The G75 star-forming region contains up to four different molecular outflows (Shepherd et al. 1997), suggesting that the 44 GHz CH$_3$OH masers could be pumped by collisions resulting from the molecular outflows. In particular, some of the methanol masers we detect are close to or within the red lobe of a molecular outflow seen in the CO (2–1) and ^{13}CO (2–1) lines (Sánchez-Monge 2011; see also Figure 7). Furthermore, the velocities of these maser components are redshifted (see Table 4) which would be expected if they are excited by collisions in the redshifted lobe of the molecular outflow.

3.4. Radio Recombination Line Emission

We used the OVRO interferometer to observe the RRLs at 3 mm (H40α) and 1 mm (H30α) toward G75, to determine the contribution of the ionized gas component at millimeter wavelengths. However, we did not clearly detect either of these lines. The spectra are dominated by continuum emission coming from either dust or ionized gas (see Section 4). Our 1σ rms noise levels for the line (continuum-free emission) are 10 and 15 mJy beam^{-1} for the H40α and H30α, respectively. Although we did not detect the RRLs, the upper limits can be used to constrain the emission from ionized gas in the millimeter range (see Section 5.2 for more details).

4. FLUX DENSITY DISTRIBUTIONS

In Figures 5 and 6, we show the flux density distributions (FDDs) of the radio continuum sources found toward G75. The UCHII source has a flat distribution, with a spectral index (α; $S_\nu \propto \nu^\alpha$) of −0.19 ± 0.06, typical of optically thin free–free emission. This FDD is well fit by an optically thin H II region with an electron density of 3.7×10^4 cm^{-3}, a diameter of ∼0.019 pc (∼3800 AU; consistent with the observed deconvolved size), and ionized by a B0 type star. In Table 5, we list the main physical parameters of the cometary UCH II region. The emission detected at 3.1 mm and the upper limit at 1.3 mm are consistent with the millimeter continuum emission coming from ionized gas, suggesting that almost no dust emission is associated with the cometary UCH II region, in agreement with Riffel & Lüdke (2010).

The eastern continuum source (EAST), barely resolved (cf. Figure 2 and Table 3), has a flat spectral index (α = −0.16 ± 0.12). Its FDD (see Figure 5) can be fit, at centimeter wavelengths, by an optically thin H II region with diameter ∼0.004 pc (900 AU; consistent with the deconvolved size listed in Table 3) and an electron density of 1.3×10^5 cm^{-3}, requiring the equivalent of at least one B0.5 star to provide the ionizing photon flux. Its physical parameters are listed in Table 5. At 3.1 mm, there is an excess of continuum emission with respect to the optically thin H II region assumption, probably coming from a dust envelope of ∼15–36 $M_\odot$ (see last column in Table 5). We refrain from fitting a dust envelope to the millimeter points of the FDD, because we have only an upper limit at 1.3 mm. Instead, we estimate an upper limit for the dust emissivity index $\beta < 1.4$, from the 3 mm detection and the 1 mm upper limit.

Finally, we construct the FDD for the CORE source, first including all the emission and then for CORE-N and CORE-S
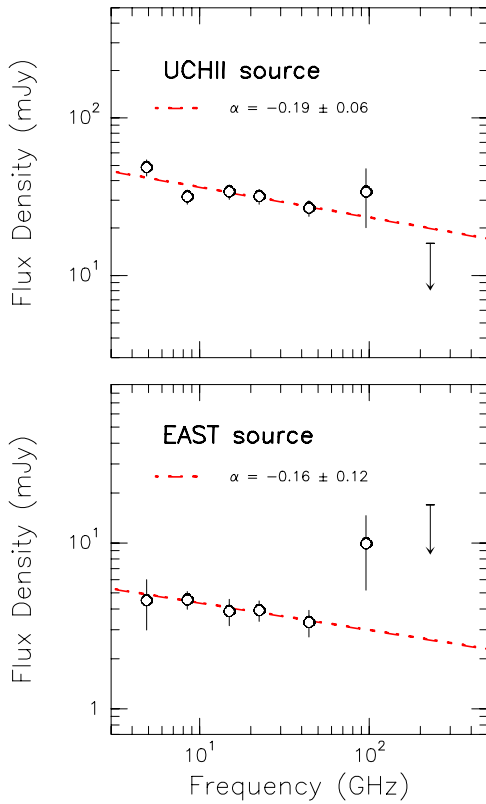
Figure 5. Spectral energy distributions for UCHII (top) and EAST (bottom) sources. Circles and upper limits correspond to the observational data from Table 3. Red dashed lines: linear fit ($S_\nu \propto \nu^\alpha$) to the centimeter data (from 6 up to 0.7 cm; see Table 5).

(A color version of this figure is available in the online journal.)
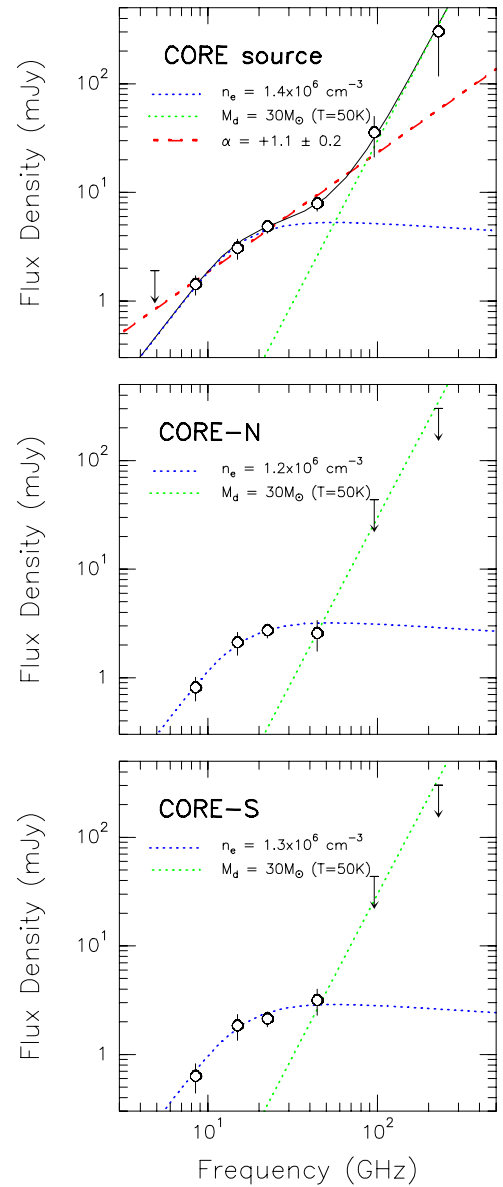

Figure 6. Flux density distributions for CORE (top), CORE-N (middle), and CORE-S (bottom) sources. Circles and upper limits correspond to the data from Table 3. Red dashed lines: linear fit ($S_\nu \propto \nu^\alpha$) to the centimeter data (from 6 to 0.7 cm; see Table 5). Blue dotted lines: homogeneous H II region with an electron density specified in the panel. Green dotted lines: modified blackbody law for the dust envelope with a dust emissivity index of $\beta = 1$, a source radius of 3″, a dust temperature of 50 K, a dust mass of 30 $M_\odot$, and a dust mass opacity coefficient of 0.9 cm^2 g^{-1} at 1.3 mm (Ossenkopf & Henning 1994).

(A color version of this figure is available in the online journal.)

separately (Figure 6). At centimeter wavelengths, the emission is partially optically thick, with a spectral index of $+1.1 \pm 0.2$ for the total emission of the CORE. The major difference between the FDDs of CORE, CORE-N, and CORE-S is the flux density at 7 mm. However, in all cases the centimeter emission can be well fit by an H II region with an electron density of $\sim 10^6$ cm^{-3} and a size <0.001 pc (<200 AU; see Table 5). An H II region with these properties has a spectral turnover in the centimeter regime. At millimeter wavelengths, where we spatially resolve the contributions of CORE-N and CORE-S, the emission is dominated by hot dust; we estimate an envelope mass of 30 $M_\odot$ for a temperature of 50 K (see Table 5).

5. NATURE OF THE IONIZED GAS EMISSION

We report the detection of four distinct radio continuum sources toward the high-mass star-forming region G75: UCHII, EAST, CORE-N, and CORE-S (the latter two correspond to the CORE source for angular resolutions coarser than 0″.3). In this section, we discuss the nature of these four sources.

5.1. UCHII and EAST: two ultracompact H II regions

The UCHII and EAST sources can be well characterized as homogeneous H II regions with sizes (3800 AU and 900 AU) and electron densities (3.7×10^4 cm^{-3} and 1.3×10^5 cm^{-3}) characteristic of small ultracompact H II regions (e.g., Kurtz 2005). They are probably ionized by B0 and B0.5 zero-age main sequence (ZAMS) stars, respectively, and are optically thin at centimeter wavelengths (i.e., spectral index of -0.1; see Table 5). Despite these similarities, the two sources are

distinctly different in their infrared emission. In particular, there is substantial IR dust emission associated with the EAST source but not with the UCHII source. In Figure 7, we show infrared and submillimeter images of the G75 star-forming complex. Infrared emission between 2.2 and 8.0 μm is clearly associated with the EAST source, while no infrared emission at these wavelengths is associated with the cometary UCHII source (cf. close-up views in Figure 7). The absence of infrared emission from the UCHII source is unusual; ultracompact H II regions typically present substantial IR emission (Hoare et al. 2007). A possible explanation is that the UCH II region may be partially obscured by a cloud of gas and dust that absorbs the near- and mid-infrared emission. In fact, such a cloud is seen in emission at

Table 5
Physical Parameters of the H II Regions and Dust Properties for the Sources in G75.78+0.34

Source	H II Region Physical Parameters[a]						Dust[b]		
	Diameter (AU)	EM (cm^{-6} pc)	n_e (cm^{-3})	M_i ($M_\odot$)	$\dot{N}_i$ (s^{-1})	Spectral Type	$S_{\nu 3mm}^{dust}$ (mJy)	$S_{\nu 1mm}^{dust}$ (mJy)	M_{dust}[c] ($M_\odot$)
UCH II	3800	2.5×10^7	3.7×10^4	4.7×10^{-3}	4.2×10^{46}	B0	7	…	…
EAST	900	6.6×10^7	1.3×10^5	1.4×10^{-4}	4.4×10^{45}	B0.5	8	<12	15–36
CORE	<200	>2.1×10^9	>1.4×10^6	<2.9×10^{-5}	1.1×10^{46}	B0.5	30	190	30
							5	110	17
CORE-N	<200	>1.2×10^9	>1.2×10^6	<1.4×10^{-5}	4.2×10^{45}	B0.5	<40	<200	<30
CORE-S	<200	>1.4×10^9	>1.3×10^6	<1.3×10^{-5}	4.1×10^{45}	B0.5	<40	<200	<30

Notes.
[a] Physical parameters of the H II regions assuming homogeneous ionized gas. For the EAST and UCH II sources, the parameters were obtained by fitting an optically thin H II region at all centimeter wavelengths, and for the CORE, CORE-N, and CORE-S sources the parameters correspond to the fit of a homogeneous H II region at all centimeter wavelengths (see Figure 5). The fit of a homogeneous H II region is obtained from the expression

$$S_\nu = B_\nu(T_e)(1 - e^{-\tau_{ff}(\nu)})\Omega_{source} = \frac{2h\nu^3}{c^2}\frac{1}{e^{h\nu/kT_e} - 1}(1 - e^{-\tau_{ff}(\nu)})\Omega_{source}, \qquad (1)$$

where S_ν is the flux density at frequency ν, $B_\nu(T_e)$ is the Planck function corresponding to the electronic temperature T_e assumed to be 10^4 K, Ω_{source} is the source solid angle, and $\tau_{ff}(\nu)$ is the optical depth defined by $\tau_{ff}(\nu) \approx 0.08235[EM/cm^{-6} pc][T_e/K]^{-1.35}[\nu/GHz]^{-2.1}$ (Altenhoff et al. 1960). The free parameters in the fit are the emission measure and the size of the source. The spectral type is determined from Panagia (1973) using the number of ionized photons, $\dot{N}_i$.
[b] $S_{\nu 3mm}^{dust}$ and $S_{\nu 1mm}^{dust}$ correspond to the (dust) millimeter continuum flux density after subtracting the contribution from free–free emission (from the fits shown in Figure 5). For the CORE source, the first value assumes the centimeter emission is described by a homogeneous H II region, and the second value assumes the centimeter emission is fitted with a power-law fit ($S_\nu \propto \nu^\alpha$) with $\alpha = 1.1$.
[c] Dust and gas mass estimated from the millimeter emission (after subtracting the contribution of the ionized gas). For the UCH II source, all the millimeter continuum emission is thermal ionized gas emission. For the EAST source, we assumed a dust emissivity index of 1.5, a dust mass opacity coefficient of 0.9 cm^2 g^{-1} at 1.3 mm (Ossenkopf & Henning 1994), and a dust temperature of 50 and 20 K, respectively. For CORE, CORE-N, and CORE-S sources, we provide the mass estimated assuming a dust emissivity index of 1, a dust mass opacity coefficient of 0.9 cm^2 g^{-1} at 1.3 mm, and a dust temperature of 50 K. The upper limits are due to the low angular resolution at millimeter wavelengths that does not allow to resolve the CORE-N and CORE-S sources.

submillimeter wavelengths (cf. emission at 450 and 850 μm in Figure 7; Di Francesco et al. 2008), and in absorption at infrared wavelengths (cf. obscured region in the infrared maps in Figure 7), and its peak falls very close to the UCHII source. In addition, if the EAST source were located closer to the border of the dust cloud (seen in the 450 μm and 850 μm images), its IR emission would be less obscured than that of the UCHII source, resulting in the different infrared properties of the two sources. The non-detection of UCHII at 1.3 mm (see Figure 3) does not contradict this scenario; as we noted in Section 3.2, the non-detection is probably due to inadequate sensitivity.

5.2. CORE: Hypercompact H II Regions or Shocks?

Regarding the emission from the CORE (N and S) source, we examine several models to explain the origin of the ionized gas emission. Franco et al. (2000) modeled the CORE source as an H II region with a density distribution $n_e \propto r^{-4}$, motivated by optically thick centimeter continuum emission at frequencies up to ∼100 GHz. Our new, higher resolution observations suggest that the emission becomes optically thin at frequencies ∼30 GHz. Figure 6 suggests that a homogeneous density distribution can account for the emission from the N and S sources. Furthermore, the RRL upper limits are also consistent with optically thin emission. Assuming optically thin emission for line and continuum, and 3σ upper limits for H30α and H40α (i.e., 30 and 45 mJy beam^{-1}, respectively), we can calculate the expected continuum emission from ionized gas with (Rohlfs &

Wilson 2004)

$$\left[\frac{S_L}{S_C}\right] = 6940\left[\frac{\Delta v}{km\ s^{-1}}\right]^{-1}\left[\frac{T_e}{K}\right]^{-1.15}\left[\frac{\nu}{GHz}\right]^{1.1}, \qquad (2)$$

where S_L is the line flux density, S_C is the continuum flux density, Δv is the width of the RRL (assumed to be 30 km s^{-1}; Kurtz 2005), T_e is the electron temperature assumed to be 10^4 K, and ν is the frequency of the line. We find that the continuum flux density of ionized gas at 3 and 1 mm should be <30 and <18 mJy, respectively. These values are in agreement with the homogeneous H II region fits given in Section 4, for which the expected flux densities at 3 and 1 mm are ∼3 mJy (i.e., ≪18 mJy). Thus, we conclude that the ionized gas emission becomes optically thin for frequencies >30 GHz. This new result, compared to Franco et al. (2000), arises because we resolve the CORE source into two components.

From the FDD analysis (see Section 4), both sources (CORE-N and S) appear to be HC H II regions ionized by B0.5 ZAMS stars, and separated by a distance of 0″.36 (1400 AU at a distance of 3.8 kpc). This scenario suggests a wide, massive binary system (Sana & Evans 2011). We searched the literature for similar systems, with two close massive radio continuum sources, and found several examples: in G31.41+0.31 there is a system of two centimeter continuum sources separated by 0″.19 (1500 AU at 7.9 kpc; Araya et al. 2008); in G10.47+0.03 there are two similar sources separated by 0″.53 (5700 AU at 10.8 kpc; Cesaroni et al. 2010); and in DR21(OH) a similar system is separated by 0″.45 (900 AU at 2 kpc; Araya et al. 2009). Thus, it seems that it is not unusual to detect double radio continuum sources, separated by ∼2000 AU, in massive star-forming regions.
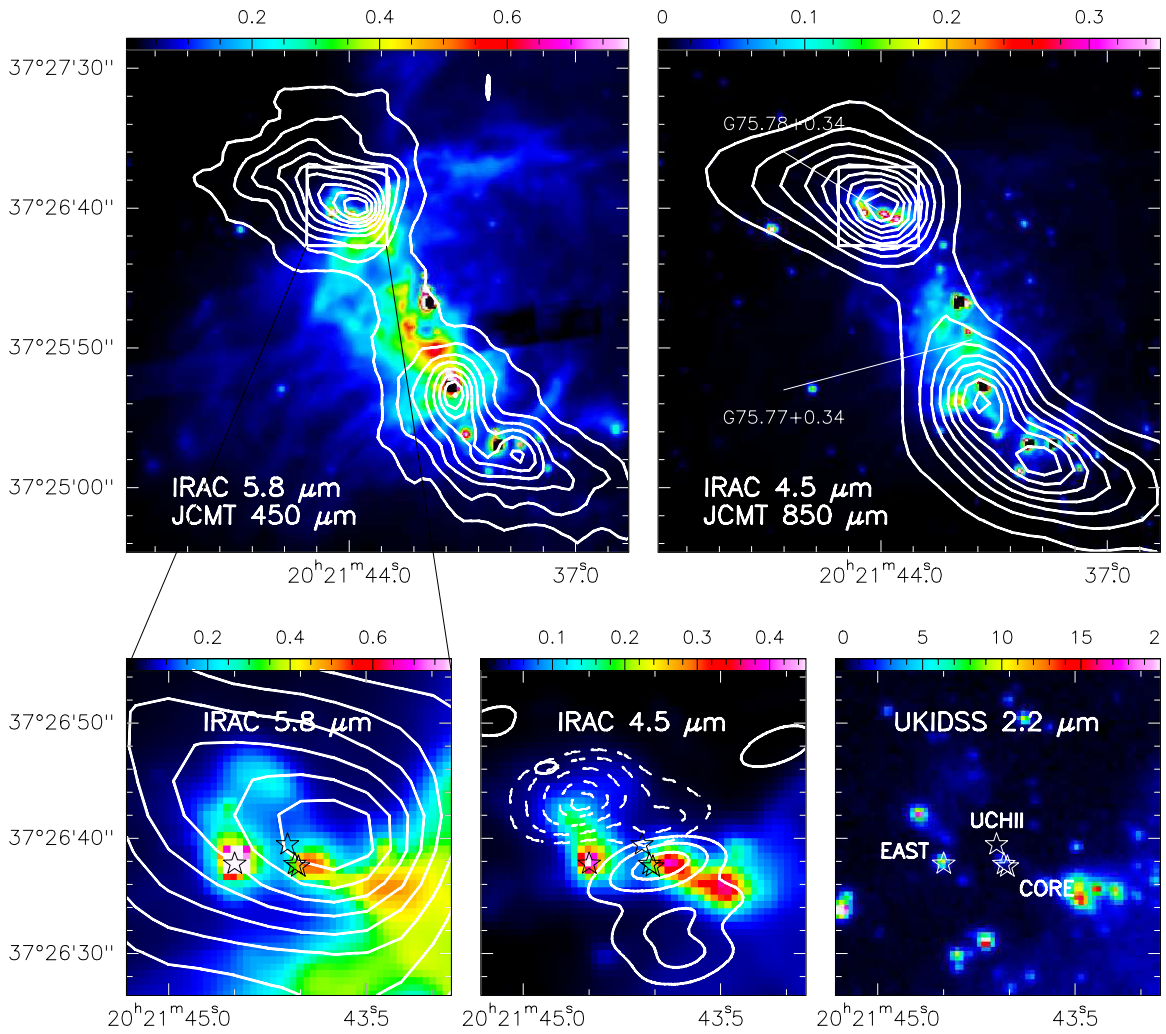
Figure 7. Submillimeter (James Clerk Maxwell Telescope (JCMT)) and infrared (*Spitzer* and UKIDSS) images of G75. Top left: 450 μm JCMT continuum image (white contours, levels start at 10% increasing in steps of 10% of the peak intensity 99.6 Jy) overlaid on the 5.8 μm IRAC-*Spitzer* image. Top right: 850 μm JCMT continuum image (white contours, levels start at 10% increasing in steps of 10% of the peak intensity 10.3 Jy), overlaid on the 4.5 μm IRAC-*Spitzer* image. The white box shows the region zoomed in the bottom panels. The large infrared and submillimeter source toward the southwest of the images corresponds to the H II region G75.77+0.34. A dark region is seen toward the northeast in the infrared images, coincident with the strong submillimeter emission, and associated with the G75 star-forming complex. The strongest sources in the region, including the large H II region G75.77+0.33, appear saturated (black pixels) in the *Spitzer* images. Bottom: close-up view of the region studied with interferometers showing the 5.8 μm, 4.5 μm, and 2.2 μm images. The white contours in the lower left panel show the 450 μm JCMT continuum emission as in the top panel. The solid/dashed white contours in the bottom middle panel show the blue/redshifted CO (2–1) emission (Sánchez-Monge 2011; the contours are 10, 30, 70, 120, and 150 Jy beam^{-1}km s^{-1}) tracing the molecular outflow with a direction similar to the elongation seen at 4.5 μm. The white/black stars mark the positions of the radio continuum sources: UCHII, EAST, and CORE-N and CORE-S (see Table 3). No infrared emission is associated with the UCHII source, while strong emission is coincident with the EAST source (see the main text for discussion). In all panels, the units of the color scales are 10^3 MJy sr^{-1}.

(A color version of this figure is available in the online journal.)

It should be noted that the radio continuum emission from some of the previously listed binary systems is not always interpreted as arising from photoionized H II regions. Araya et al. (2009) propose that the radio continuum emission in DR(21)OH is free–free radiation originating in interstellar shocks, following the theoretical development of Ghavamian & Hartigan (1998). In this scenario, the free–free emission arises from shock-ionized, rather than photo-ionized, gas, being comparable to the Herbig–Haro objects seen in the optical.

We note that the infrared emission at 4.5 μm (see Figure 7) shows an elongated structure "emanating" from the position of the CORE source. The fluxes of this structure in the four IRAC/*Spitzer* bands are 4 mJy at 3.6 μm, 52 mJy at 4.5 μm, 96 mJy at 5.8 μm, and 115 mJy at 8.0 μm, and thus it fulfills the

criteria[11] defined by Chambers et al. (2009) to be classified as a "green fuzzy" (see also Cyganowski et al. 2008). The excess 4.5 μm emission can be produced by shocks associated with outflows, scattered continuum in outflow cavities, obscuration affecting the emission at 3.6 μm, or fluorescence H$_2$ emission (e.g., Noriega-Crespo et al. 2004; Smith et al. 2006; Qiu et al. 2008; De Buizer & Vacca 2010; Takami et al. 2010, 2012; Varricatt 2011; Simpson et al. 2012; Lee et al. 2012), and only spectroscopic studies in the mid-infrared can clearly determine the origin of the 4.5 μm excess. However, in G75, the northeast–southwest direction of the 4.5 μm elongated

---

[11] Chambers et al. (2009) classified an extended mid-infrared source as a "green fuzzy" according to the following color criteria: (1) the 4.5 μm to 3.6 μm flux ratio is ⩾1.8, (2) the 4.5 μm to 5.8 μm flux ratio is ⩾0.40, and (3) the 4.5 μm to 8.0 μm flux ratio is ⩾0.45.

structure is consistent with the direction of the molecular outflow likely associated with the CORE source (see the solid/dashed contours in the bottom middle panel of Figure 7; Sánchez-Monge 2011) which is also consistent with the direction of the outflow reported by Riffel & Lüdke (2010) at larger scales, thus favoring the interpretation of the 4.5 μm emission arising from shocks. In addition, the spatial distribution of water masers (Figure 4) is also indicative of shocks and jets, as found in other star-forming regions (e.g., IRAS 20126+4104: Hofner et al. 2007). A milliarcsecond kinematical study of water masers in G75.78+0.34 (see Figure 3 in Ando et al. 2011) is consistent with a shock interpretation for the centimeter continuum emission. The group of masers associated with CORE-S have velocities mainly in the southwest direction (similar to the elongated structure seen at 4.5 μm), while the two groups of maser spots located to the northwest and southeast of CORE-S show a velocity field suggesting expansion. Together with the arc morphology of all the maser spots, this is suggestive of a bow-shock, implying that at least the CORE-S emission might arise from shocks.

A stellar jet/outflow with a mass-loss rate larger than 410^{-6} $M_\odot$ yr^{-1} and a terminal velocity of order several hundred km s^{-1}, shocking the ambient medium, would have sufficient energy to ionize, heat, and move the gas of both the CORE-N and CORE-S sources (see the Appendix). Although the cooling time (and hence recombination) of the high-density gas is very short (Franco et al. 1994), the jet/outflow would continuously re-ionize the material. In this case, the exciting source would be located between the two radio continuum sources, with its own H II region quenched by the high-density medium. I.e., a jet/outflow with such a high mass-loss rate would be neutral because the ionization front would be trapped very close to the star. The possibility of a neutral jet/outflow shocking the ambient gas cannot currently be ruled out because our observations are sensitive to ionized gas. This scenario can be tested with future centimeter continuum observations with the JVLA, to determine if CORE-S (and the water maser spots) have been displaced with respect to the other continuum sources. Assuming a jet velocity of order several hundred km s^{-1}, relative motions could be detected within the next five years.

As noted in Section 1, other mechanisms might also cause the centimeter emission from CORE-N and S. However, we consider most of these to be unlikely candidates. Equatorial winds (Hoare 2006) or thermal radio jets (Anglada 1996) typically predict constant spectral indices of +0.6 and a relation between the source size and the frequency. Our observations indicate spectral indices ∼+1; the uncertainties in the deconvolved source sizes are too large to determine a size–frequency dependence. A photoevaporated disk model has been proposed to explain the continuum emission of double-peaked sources with an hourglass morphology (Lugo et al. 2004). Although the CORE-N and S peaks might be fit as a photoevaporated disk, recent studies indicate that the peaks from photoevaporated disks should change their separation with frequency, moving closer at higher frequencies (Tafoya et al. 2004). The peak positions of N and S do not change between 3.6 and 0.7 cm to a precision of ∼0″.02.

Summarizing, the centimeter continuum emission from CORE-N and S can be well fitted by homogeneous H II regions, each one photoionized by a B0.5 ZAMS star. Alternatively, free–free radiation from shock-ionized gas resulting from the interaction of a jet/outflow system with the surrounding environment appears to be a viable scenario as well. Other possible mechanisms are deemed unlikely.

6. CONCLUSIONS

We have carried out subarcsecond angular resolution observations with the VLA in the centimeter continuum and in H$_2$O and CH$_3$OH maser emission toward the massive star-forming complex G75.78+0.34. We have complemented these observations with OVRO and SMA millimeter continuum and RRL observations, and submillimeter/infrared data from online databases. Our conclusions can be summarized as follows:

1. Our radio continuum data reveal centimeter continuum emission at all wavelengths, with the emission coming from four distinct compact sources: UCHII, EAST, CORE-N, and CORE-S. The two last sources appear unresolved (CORE source) when observed with angular resolutions ≳0″.3.

2. The strongest source, UCHII, is a cometary UCH II region with a size of 0.02 pc (3800 AU), an electron density of 3.7×10^4 cm^{-3} and is ionized by the equivalent of a B0 ZAMS star. The EAST source, located ∼6″ to the east of UCHII, is also a UCH II region with an electron density of 1.3×10^5 cm^{-3}, ionized by a B0.5 equivalent ZAMS star, but with a smaller (barely resolved) size of 0.004 pc (900 AU). The millimeter continuum emission associated with these two UCH II regions has different origins: for the UCHII source it probably traces the ionized gas, while for the EAST source there is a millimeter excess, suggesting that this source is still embedded in a compact dust clump also detectable at mid-infrared wavelengths, with a mass of 15–36 $M_\odot$. We suggest that the non-detection of thermal dust emission in the UCHII source results from foreground extinction, not from an absence of warm dust.

3. The CORE-N and S sources are located 2″ to the southwest of the cometary arc of the UCHII source, and are associated with water maser and dense molecular gas emission. The two sources are very close to one another (0″.36, 1400 AU) and have similar properties: flux density increasing with frequency, and unresolved emission. The free–free continuum emission may be produced by two HC H II regions ionized by B0.5 ZAMS stars or by the collision between a jet/outflow and the surrounding environment. A dust clump of ∼30 $M_\odot$ associated with the CORE source is detected at millimeter wavelengths.

4. We have also reported high angular resolution observations of H$_2$O and class I CH$_3$OH maser emission. The class I methanol maser spots are found far from any of the radio continuum sources, and are probably excited by collisional processes due to the presence of multiple molecular outflows. The water maser spots appear close to the CORE-N and S sources, with only a few of them spatially coincident with the S source. The spatial distribution of the water masers and the kinematics observed at milliarcsecond angular resolution suggest that they could originate in a shock between a jet/outflow and the local surroundings. In addition, extended 4.5 μm emission likely tracing shocked gas could be associated with a jet driven by the CORE source.

In summary, we have characterized the radio continuum emission toward the massive star-forming complex G75.78+0.34, revealing the presence of four sources: two ultracompact H II regions (named UCHII and EAST) ionized by B0–B0.5 ZAMS stars, one with an extended and cometary shape and the other being barely resolved; and two compact sources (named CORE-N and CORE-S) associated with at least one massive

protostar embedded in a dense and massive envelope and with hints of driving an outflow.

APPENDIX

ENERGY BUDGET

Consider a star that ejects into a cloud a bipolar jet/outflow with a mass-loss rate $\dot{M}_j$ and a jet velocity v_j. The jet will collide with the ambient material in two opposite directions and will produce two shocked ionized regions. The luminosity of the jet, L_j, is given by

$$L_j = \frac{1}{2} \dot{M}_j v_j^2 = 7.9 \times 10^{35} \left[\frac{\dot{M}_j}{10^{-5} M_\odot \, \mathrm{yr}^{-1}} \right]$$
$$\times \left[\frac{v_j}{500 \, \mathrm{km \, s}^{-1}} \right]^2 \mathrm{erg \, s}^{-1}. \qquad (A1)$$

The shocked ionized gas is postshock ambient gas pushed and heated by the stellar bipolar jet. For simplicity, we will assume both shocked ionized regions have the same physical characteristics. Then, the minimum luminosity required to keep the postshock gas ionized is

$$L_i = E_0 \dot{N}_i = 2.2 \times 10^{35} \left[\frac{\dot{N}_i}{10^{46} \, \mathrm{s}^{-1}} \right] \mathrm{erg \, s}^{-1}, \qquad (A2)$$

where $E_0 = 13.6$ eV is the ionization energy of the hydrogen atom and $\dot{N}_i$ is the rate of ionizing photons inferred from the radio continuum emission of the ionized region. Furthermore, the energy lost by radiation from each region is

$$L_{\mathrm{rad}} \sim \Lambda(T) \, V_i = 4.2 \times 10^{34} \left[\frac{n_e}{10^6 \, \mathrm{cm}^{-3}} \right]^2$$
$$\times \left[\frac{r_i}{100 \, \mathrm{AU}} \right]^3 \mathrm{erg \, s}^{-1}, \qquad (A3)$$

where we assume a cooling rate per unit volume $\Lambda(10^4 \, \mathrm{K})/(n_e n_p) \sim 3 \times 10^{-24} \mathrm{erg \, cm}^3 \, \mathrm{s}^{-1}$ (Osterbrock 1989), a volume of each region with radius r_i, $V_i = 4\pi r_i^3/3$, and assume that the electron density is equal to the proton density, $n_e = n_p$. Also, we estimate the kinetic luminosity of each ionized region

averaged over its lifetime as

$$L_K \sim \frac{M_i v_i^2}{2 \, \tau_{\mathrm{cross}}} = 1.5 \times 10^{34} \left[\frac{n_e}{10^6 \, \mathrm{cm}^{-3}} \right] \left[\frac{r_i}{100 \, \mathrm{AU}} \right]^3$$
$$\times \left[\frac{v_i}{200 \, \mathrm{km \, s}^{-1}} \right]^2 \left[\frac{\tau_{\mathrm{cross}}}{10 \, \mathrm{yr}} \right]^{-1} \mathrm{erg \, s}^{-1}, \qquad (A4)$$

where the mass of ionized gas is $M_i = m_H n_p V_i$, the velocity is v_i, and τ_{cross} is the crossing time that can be estimated from $\tau_{\mathrm{cross}} = l/v_i$, where l is the distance from the ionized region to the star emitting the jet.

We consider now the particular case of the CORE-N and CORE-S sources. From Table 5, we take $n_i \sim 10^6 \, \mathrm{cm}^{-3}$, $r_i \sim 100$ AU, and $\dot{N}_i \sim 4 \times 10^{45} \, \mathrm{s}^{-1}$. We assume that each core is the ionized working surface (WS) of the jet moving into the cloud. For strong shocks, the speed of each WS is given by ram pressure balance as $v_i = \beta v_j/(1 + \beta)$, where $\beta = \sqrt{\rho_j/\rho_a}$ is the square root of the ratio of the jet and ambient densities (e.g., Raga et al. 1990). For large jet mass-loss rates, close to the emitting source, we assume $\beta \sim 1$. Then, for a jet velocity $v_j \sim 500 \, \mathrm{km \, s}^{-1}$ (of the order of the escape speed of a 10 $M_\odot$ star assumed to be the source of the jet) the shocked ionized gas moves with a speed, $v_i \sim v_j/2 \sim 250 \, \mathrm{km \, s}^{-1}$. Because the two continuum sources are separated by $\sim$1700 AU, we assume a distance to the jet source in between CORE-N and CORE-S, $l \sim 850$ AU. Then, the resulting crossing time for both ionized regions is $\tau_{\mathrm{cross}} \sim 16.2$ yr. Introducing these values in Equations (A2)–(A4), we obtain for each shocked ionized region $L_i \approx 8.8 \times 10^{34} \mathrm{erg \, s}^{-1}$, $L_{\mathrm{rad}} \approx 4.2 \times 10^{34} \mathrm{erg \, s}^{-1}$, and $L_K \approx 1.5 \times 10^{34} \mathrm{erg \, s}^{-1}$.

Finally, one can now estimate the minimum mass-loss rate and velocity of a jet necessary to ionize, heat, and move the CORE-N and CORE-S sources. The energy budget has to fulfill the relation $L_j > 2(L_i + L_{\mathrm{rad}} + L_K)$. From Equation (A1), the minimum mass-loss rate of the bipolar jet/outflow that heats and moves the ionized regions would be $\dot{M}_j > 3.7 \times 10^{-6} M_\odot \, \mathrm{yr}^{-1}$.

REFERENCES

Altenhoff, W., Mezger, P. G., Wendker, H., & Westerhout, G. 1960, Veroff. Univ. Sternwarte Bonn, 59, 48
Ando, K., Nagayama, T., Omodaka, T., et al. 2011, PASJ, 63, 45
Anglada, G. 1996, in ASP Conf. Ser. 93, Radio Emission from the Stars and the Sun, ed. A. R. Taylor & J. M. Paredes (San Francisco, CA: ASP), 3
Araya, E., Hofner, P., Kurtz, S., Olmi, L., & Linz, H. 2008, ApJ, 675, 420
Araya, E. D., Kurtz, S., Hofner, P., & Linz, H. 2009, ApJ, 698, 1321
Ávalos, M., & Lizano, S. 2012, ApJ, 751, 63
Beuther, H., & Shepherd, D. 2005, in Cores to Clusters: Star Formation with Next Generation Telescopes, ed. M. S. N. Kumar, M. Tafalla, & P. Caselli (New York: Springer), 105
Bisschop, S. E., Fuchs, G. W., Boogert, A. C. A., van Dishoeck, E. F., & Linnartz, H. 2007, A&A, 470, 749
Briggs, D. 1995, PhD thesis, New Mexico Inst. of Mining and Technology
Campbell, M. F., Niles, D., Nawfel, R., et al. 1982, ApJ, 261, 550
Carral, P., Kurtz, S. E., Rodriguez, L. F., de Pree, C., & Hofner, P. 1997, ApJL, 486, L103
Cesaroni, R., Hofner, P., Araya, E., & Kurtz, S. 2010, A&A, 509, A50
Chambers, E. T., Jackson, J. M., Rathborne, J. M., & Simon, R. 2009, ApJS, 181, 360
Codella, C., Cesaroni, R., López-Sepulcre, A., et al. 2010, A&A, 510, A86
Cragg, D. M., Johns, K. P., Godfrey, P. D., & Brown, R. D. 1992, MNRAS, 259, 203
Cyganowski, C. J., Whitney, B. A., Holden, E., et al. 2008, AJ, 136, 2391
De Buizer, J. M., & Vacca, W. D. 2010, AJ, 140, 196
Dent, W. R. F., MacDonald, G. H., & Andersson, M. 1988, MNRAS, 235, 1397

Di Francesco, J., Johnstone, D., Kirk, H., MacKenzie, T., & Ledwosinska, E. 2008, ApJS, 175, 277
Eisloffel, J., Mundt, R., Ray, T. P., & Rodriguez, L. F. 2000, in Protostars and Planets IV, ed. V. Mannings, A. P. Boss, & S. S. Russell (Tucson, AZ: Univ. Arizona Press), 815
Elldér, J., Rönnäng, B., & Winnberg, A. 1969, Natur, 222, 67
Feigelson, E. D., & Montmerle, T. 1999, ARA&A, 37, 363
Franco, J., Kurtz, S., Hofner, P., et al. 2000, ApJL, 542, L143
Franco, J., Miller, W. W., III, Arthur, S. J., Tenorio-Tagle, G., & Terlevich, R. 1994, ApJ, 435, 805
Garay, G. 1987, RMxAA, 14, 489
Ghavamian, P., & Hartigan, P. 1998, ApJ, 501, 687
Hanson, M. M., Luhman, K. L., & Rieke, G. H. 2002, ApJS, 138, 35
Hoare, M. G. 2006, ApJ, 649, 856
Hoare, M. G., Kurtz, S. E., Lizano, S., Keto, E., & Hofner, P. 2007, in Protostars and Planets V, ed. B. Reipurth, D. Jewitt, & K. Keil (Tucson, AZ: Univ. Arizona Press), 181
Hofner, P., Cesaroni, R., Olmi, L., et al. 2007, A&A, 465, 197
Hofner, P., & Churchwell, E. 1996, A&AS, 120, 283
Hollenbach, D., Johnstone, D., Lizano, S., & Shu, F. 1994, ApJ, 428, 654
Keto, E. 2002, ApJ, 568, 754
Keto, E. 2003, ApJ, 599, 1196
Keto, E. 2007, ApJ, 666, 976
Klaassen, P. D., & Wilson, C. D. 2007, ApJ, 663, 1092
Kurtz, S. 2005, in IAU Symp. 227, Massive Star Birth: A Crossroads of Astrophysics, ed. R. Cesaroni, M. Felli, E. Churchwell, & M. Walmsley (Cambridge: Cambridge Univ. Press), 111
Kurtz, S., Hofner, P., & Álvarez, C. V. 2004, ApJS, 155, 149
Lee, H.-T., Takami, M., Duan, H.-Y., et al. 2012, ApJS, 200, 2
Lugo, J., Lizano, S., & Garay, G. 2004, ApJ, 614, 807
Matthews, H. E., Goss, W. M., Winnberg, A., & Habing, H. J. 1973, A&A, 29, 309
Matthews, H. E., Goss, W. M., Winnberg, A., & Habing, H. J. 1977, A&A, 61, 261
Matthews, N., Anderson, M., & MacDonald, G. H. 1986, A&A, 155, 99
Mezger, P. G., & Henderson, A. P. 1967, ApJ, 147, 471
Nagayama, T., & VERA project members 2012, in IAU Symp. 287, Cosmic Masers—from OH to H0, ed. R. S. Booth, W. H. T. Vlemmings, & E. M. L. Humphreys (Cambridge: Cambridge Univ. Press), 391
Noriega-Crespo, A., Morris, P., Marleau, F. R., et al. 2004, ApJS, 154, 352
O'Dell, C. R., & Wong, K. 1996, AJ, 111, 846
Olmi, L., & Cesaroni, R. 1999, A&A, 352, 266
Olnon, F. M. 1975, A&A, 39, 217
Ossenkopf, V., & Henning, T. 1994, A&A, 291, 943

Osterbrock, D. E. 1989, Research supported by the University of California, John Simon Guggenheim Memorial Foundation, University of Minnesota et al. (Mill Valley, CA: Univ. Science Books), 422
Panagia, N. 1973, AJ, 78, 929
Panagia, N., & Felli, M. 1975, A&A, 39, 1
Pratap, P., Shute, P. A., Keane, T. C., Battersby, C., & Sterling, S. 2008, AJ, 135, 1718
Qiu, K., Zhang, Q., Megeath, S. T., et al. 2008, ApJ, 685, 1005
Raga, A. C., Binette, L., Cantó, J., & Calvet, N. 1990, ApJ, 364, 601
Reid, M. J., Argon, A. L., Masson, C. R., Menten, K. M., & Moran, J. M. 1995, ApJ, 443, 238
Riffel, R. A., & Lüdke, E. 2010, MNRAS, 404, 1449
Roberts, H., & Millar, T. J. 2007, A&A, 471, 849
Rodríguez, L. F., Curiel, S., Moran, J. M., et al. 1989, ApJL, 346, L85
Rodríguez, L. F., Garay, G., Brooks, K. J., & Mardones, D. 2005, ApJ, 626, 953
Rodríguez, L. F., González, R. F., Montes, G., et al. 2012, ApJ, 755, 152
Rodríguez, L. F., Marti, J., Canto, J., Moran, J. M., & Curiel, S. 1993, RMxAA, 25, 23
Rohlfs, K., & Wilson, T. L. (ed.) 2004, Tools of Radio Astronomy (4th rev. and enl. Berlin: Springer)
Rygl, K. L. J., Brunthaler, A., Sanna, A., et al. 2012, A&A, 539, A79
Sana, H., & Evans, C. J. 2011, in IAU Symp. 272, Active OB Stars: Structure, Evolution, Mass Loss, and Critical Limits, ed. C. Neiner, G. Wade, G. Meynet, & G. Peters (Cambridge: Cambridge Univ. Press), 474
Sánchez-Monge, Á. 2011, PhD thesis, Universitat de Barcelona
Shchekinov, Y. A., & Sobolev, A. M. 2004, A&A, 418, 1045
Shepherd, D. S., Churchwell, E., & Wilner, D. J. 1997, ApJ, 482, 355
Shepherd, D. S., & Kurtz, S. E. 1999, ApJ, 523, 690
Shirley, Y. L., Evans, N. J., II, Young, K. E., Knez, C., & Jaffe, D. T. 2003, ApJS, 149, 375
Simpson, J. P., Cotera, A. S., Burton, M. G., et al. 2012, MNRAS, 419, 211
Smith, H. A., Hora, J. L., Marengo, M., & Pipher, J. L. 2006, ApJ, 645, 1264
Tafoya, D., Gómez, Y., & Rodríguez, L. F. 2004, ApJ, 610, 827
Takami, M., Chen, H.-H., Karr, J. L., et al. 2012, ApJ, 748, 8
Takami, M., Karr, J. L., Koh, H., Chen, H.-H., & Lee, H.-T. 2010, ApJ, 720, 155
Varricatt, W. P. 2011, A&A, 527, A97
Wood, D. O. S., & Churchwell, E. 1989, ApJS, 69, 831
Zapata, L. A., Rodríguez, L. F., Ho, P. T. P., Beuther, H., & Zhang, Q. 2006, AJ, 131, 939
Zapata, L. A., Rodríguez, L. F., Kurtz, S. E., & O'Dell, C. R. 2004, AJ, 127, 2252